Progress In Electromagnetics Research B, Vol. 38, 107–134, 2012

COMBINING ADVANCES IN EM INDUCTION INSTRUMENTATION AND INVERSION SCHEMES FOR UXO CHARACTERIZATION

C. P. Oden*

Earth Science Systems, LLC, 11485 W. I-70 Frontage Rd., Unit B, Wheat Ridge, CO 80033, USA

Abstract—Several experimental time-domain EM induction instruments have recently been developed for unexploded ordnance (UXO) detection and characterization that use multiple transmitting and receiving coil combinations. One such system, the US Geological Survey's ALLTEM system, is unique in that it measures both the electrodynamic response (i.e., induced eddy currents) and the magneto-static response (i.e., induced magnetization). This allows target characterization based on the dyadic polarizability of both responses. This paper examines the numerical response of the ALLTEM instrument due to spheroidal, conductive, and permeable UXO targets; and to conductive and optionally viscous magnetic earth. An inversion scheme is presented for spheroidal targets that incorporates fully polarimetric measurements for both magneto-static and electro-dynamic excitations. The performance of the inversion algorithm is evaluated using both simulated and surveyed data. The results are examined as a function of the number of coil combinations, number of instrument locations, and uncertainty in sensor location and orientation. Results from the specific cases tested (prolate spheroids lying horizontally) show that 1) that collecting data from more than 12 sensor locations or from more than four coil combinations reduced the chances that inversion solutions would be from a local minimum, and 2) that uncertainties in position greater than 3 cm or in orientation greater than 10 degrees cause errors in the estimated spheroid principal lengths of greater than 100%. Soil conductivities less than 1 S/m contribute negligible interference to the target response, but viscous magnetic soils with permeabilities greater than 10^{-6} MKS units do cause detrimental interference.

Received 26 November 2011, Accepted 9 January 2012, Scheduled 13 January 2012

* Corresponding author: Charles P. Oden (coden@earthsciencesystems.com).

1. INTRODUCTION

Over the last decade, there have been many advances in magnetic and electromagnetic (EM) induction methods for detecting and characterizing unexploded ordnance (UXO). These advances illustrates that no single innovation best solves this difficult problem, but that a combination of the best aspects of these techniques are needed. We begin by reviewing notable instruments and algorithms that have been developed over the last decade, and then discuss a combination of key advances that enhance detection and discrimination.

EM induction instruments apply time varying magnetic fields (i.e., primary fields) that induce eddy currents in the target. These induced currents produce secondary magnetic fields whose characteristics depend on the shape and electromagnetic properties of the target. The broadband response from time-domain EM induction instruments such as the Geonics EM-63 contains information about the shape and composition of buried metallic objects (i.e., targets) that is difficult to obtain with frequency-domain instruments operating at one frequency [1]. Similar information is also available from wideband frequency-domain instruments such as the Geophex GEM-3 [2, 3]. In recent years, algorithms have been developed to estimate the location, shape, and composition (ferrous or non-ferrous metal) of targets using data from these broadband systems [4, 5].

The previously mentioned instruments are not fully polarimetric because they only have a single transmitting coil at a fixed orientation, and one or more receiving coils at fixed orientations. A single transmitting coil can subject the target to primary fields in three orthogonal directions, but only by moving the coil to several locations. Certain primary field polarizations at the target require the instrument to be offset from the target, which results in lower intensity excitation and reduced sensitivity to induced currents. A fully polarimetric system has multiple transmitting coils that can subject the target to primary fields with components in three orthogonal directions while the instrument is at a single location. When operating each of the transmitting coils, multiple receiving coils measure all three components of the secondary magnetic fields generated by the target. A total of six linearly independent measurements are routinely made with fully-polarimetric systems by operating different transmitting and receiving coil combinations. Fully polarimetric datasets greatly reduce ambiguity in target characterization [6, 7]. Examples of fully-polarimetric systems include the U.S. Geological Survey's ALLTEM system [8], the Berkeley UXO Discriminator [9], and the MetalMapper (D. Snyder and D. George, pers. comm., November 2009).

Many algorithms have been created to estimate the shape of UXO targets from EM induction measurements [6, 10–12], and passive magnetic measurements [13, 14] based on the target's equivalent induced dipole moments. It has been shown that the uncertainty in estimated target shapes is reduced by analyzing datasets from both EM induction sensors and passive magnetometers [10, 15]. Consequently, several instrument platforms have been built incorporating both EM induction and passive magnetic measurements; these include the Advanced Ordinance Locator [16], and the Multi-sensor Towed Array Detection System (MTADS) [17].

There is an inherent ambiguity in target shape estimates based on measurements from single-coil-pair metal detectors because the magnetic fields from the transmitting coil only penetrate the target with a limited range of directions [18]. The situation is worse with passive magnetic data because the earth's magnetic field only penetrates the target in a single direction [13]. Spheroidal targets with different shapes and sizes can produce the same induced dipole moment due to the earth's field, which makes characterization difficult. These difficulties are ameliorated by making active fully-polarimetric measurements at each instrument location that 1) induce magnetization in each orthogonal direction of ferrous targets, and/or 2) induce eddy currents in each orthogonal plane of conductive targets. In this paper, we refer to this induced magnetization as the magneto-static response, and the induced eddy currents as the electro-dynamic response.

Under ideal circumstances, the algorithms cited above perform well in their characterization of UXO, however common environmental conditions exist that reduce the effectiveness of these methods. For instance, the effects of the medium surrounding the target can interfere with detection and characterization. This medium can have variable conductivity, magnetic susceptibility, and magnetic viscosity [24]. The effects of these properties are referred to as geologic noise. Another adverse condition is the variable and uncertain position and orientation of the survey instrument that results when acquiring data from a sensor moving over ground with small scale variations in surface topography. Finally, the signals from deep targets can be too small for proper characterization. For example, UXO targets deeper than about 1.5 meters are generally difficult to characterize with the ALLTEM system [19].

This paper analyzes data from the ALLTEM instrument because it uniquely combines the desirable aspects of being broadband, fully polarimatric, and makes both magneto-static and electro-dynamic measurements. We begin by modeling the ALLTEM response and

investigating the effects of various adverse environmental effects. Next, we present an inversion method to estimate the composition and shape of targets that makes use of both the electro-dynamic and magneto-static measurements taken from many instrument locations. This inversion method is evaluated using modeled data and collected data. The adverse effects of uncertainty in sensor position and orientation, as well as EM noise are examined. Finally, the benefits of adding more time-gates, spatial samples, and transmitting and receiving polarization combinations are studied. To the author's knowledge, the combination of all of these desirable aspects in instrumentation and analysis has not been previously studied.

2. ALLTEM MODELING

The ALLTEM induction system uses a triangle wave transmitter waveform that excites both a transient electro-dynamic response and a magneto-static response [8]. The instrument has a coil array contained on a one-meter square cube (see Figure 1). To conduct a survey along a line on the earth's surface, the cube is held at a height of 17 cm (typically) above the surface and is moved along the ground surface. Adjacent lines are run so that no subsurface target is horizontally offset from the cube center by more than 50 cm. The volume of investigation is horizontally delimited by the extent of the survey lines and extends down to a depth of one meter (typical targets are less than a meter deep). Although numerous coil combinations are possible, in the standard configuration the instrument records data from 19 standard transmitting-receiving coil combinations which are described in Appendix B. Figure 1 shows two of these coil combinations — one using vertical magnetic dipoles (VMDs) and the other using horizontal magnetic dipoles (HMDs). A given coil configuration uses one transmitting coil midway between two receiving coils in a gradiometer configuration. The result is that the receiver gradiometer cancels the primary signal from the transmitter coil.

The ALLTEM instrument responds both to metallic targets and their host soils. Accordingly, we begin by modeling the ALLTEM response to a conductive, magnetic, and optionally a viscous magnetic earth. The integral expressions for the magnetic fields generated by infinitely small VMDs and HMDs over a conductive magnetic half space are given in [20, 21]. These integrals are numerically evaluated using a fast Hankel transform [22] to produce Green's functions for the magnetic field due to a dipole over a half-space. The ground response at a given receiver coil due to excitation by a given transmitter coil is

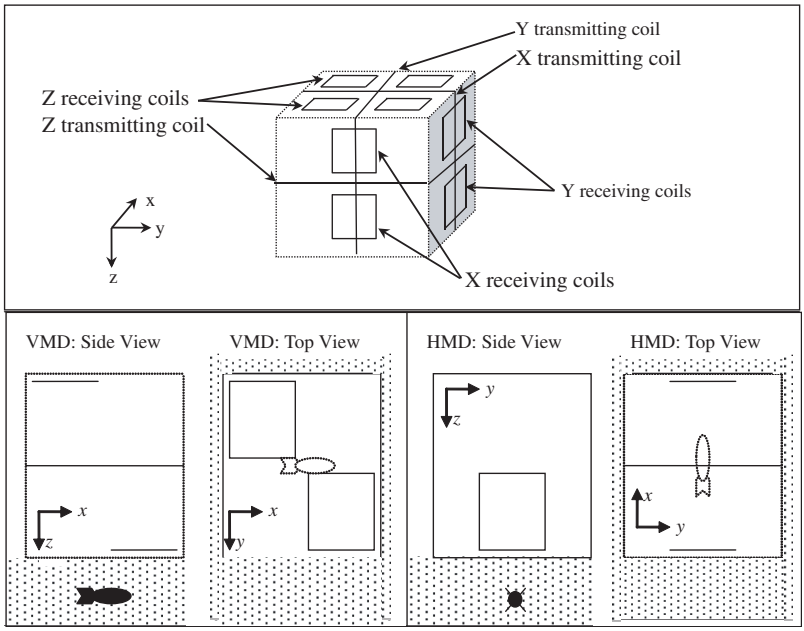

Figure 1. ALLTEM cube showing coil arrangements. The top panel shows the locations of the transmitting and receiving coils. Opposite cube faces have identical coil arrangements. Each coil combination has a 1.0 meter square transmitter loop, and two 0.35 meter square receiver loops (solid lines). The bottom left panel shows side view and top view of a VMD coil combination that has a large VMD transmitter coil midway between two smaller VMD receiver coils. The bottom right panel shows side view and top view of a HMD coil combination, which has a large HMD transmitter coil midway between two smaller HMD receiver coils. The z axis is positive down. Dashed lines show the outline of the one meter cube containing the coils, and of the UXO target.

calculated by numerically evaluating the following integrals,

$$V_{rx}(\omega) = -i\omega T(\omega) \cdot \int\limits_{RXloop} \hat{n}_{rx} \cdot \int\limits_{TXloop} \hat{n}_{tx} \cdot \overleftrightarrow{G}^{-}(\sigma, \mu, \vec{r}, \vec{r}\,')d\vec{r}d\vec{r}\,', \quad (1)$$

where $T(\omega)$ is the Fourier transform of the transmitter excitation (a triangle wave), $\overleftrightarrow{G}^{-}(\sigma, \mu, \vec{r}, \vec{r}\,')$ is the dyadic Green's function for the fields above the surface due to a dipole moment above the surface (see Appendix A), σ is the ground conductivity, μ is magnetic permittivity

(possibly complex and frequency dependent), ω is radian frequency, V_{rx} is the voltage at the receiver coil, $\hat{n}_{tx}$ and $\hat{n}_{rx}$ are the normals to the planes containing the transmitting and receiving coils, and the integrals are over the area of the transmitting and receiving coils. This procedure is used to calculate the voltage at each receiving coil in the gradiometer, and the simulated result is the difference between these coil voltages. Finally, the frequency-domain coil voltage is converted into a time-domain signal using a numerical Fourier transform (FFT).

Modeling the response of a conductive permeable spheroid is slightly more involved. First, the magnetic field below the surface is calculated at the center of the target using (2). Here the dyadic Green's function is now for the fields below the surface due to a dipole moment above the surface (see Appendix A),

$$\vec{H}_0(r,\omega) = T(\omega) \int\limits_{TXloop} \hat{n}_{tx} \cdot \overleftrightarrow{G}^{+}(\sigma,\mu,\vec{r},\vec{r}\,')d\vec{r}\,'. \tag{2}$$

Next, assuming that the primary field is constant throughout the target, the equivalent induced dipole moment $\vec{m}(\omega)$ for the target centered at r is calculated,

$$\vec{m}(\omega) = \overleftrightarrow{R}^{T} \cdot \overleftrightarrow{M}(\omega) \cdot \overleftrightarrow{R} \cdot \vec{H}_0(r,\omega), \tag{3}$$

where $\overleftrightarrow{M}(\omega)$ is the diagonal frequency-dependent magnetic-polarizability tensor. Calculations for specifying this tensor for conductive permeable prolate and oblate spheroids are given in [23]. $\overleftrightarrow{R}$ is a rotation matrix that converts the magnetic field to target spheroid centric coordinates. Note that for a given incident field, only a single component of the polarizability tensor is excited. A fully polarimetric instrument switches through different coil configurations resulting in incident fields with components in all possible directions. The result is that all components of the polarizability tensor are excited, which provides more information about the target.

The final step is to calculate the fields at the receiver coils due to the induced dipole moments at the target. Using the reciprocity theorem, we find that the voltage induced in the receiver coil V_{rx} due to the induced target dipole moment $\vec{m}$ is related to the magnetic field $\vec{H}_{rx}$ at the target due to a test current (taken to be unity) in the receiver coil I_{rx},

$$V_{rx}(\omega) = -i\omega \frac{\mu \vec{H}_{rx} \cdot \vec{m}(\omega)}{I_{rx}}. \tag{4}$$

Equation (2) is used to calculate the magnetic field at the target, only now the integral is over the area of the receiver coil. As before, this

procedure is used to calculate the voltage at each receiving coil in the gradiometer, and the simulated result is the difference between these coil voltages. Finally, the frequency-domain coil voltage is converted into a time-domain signal using a numerical Fourier transform (FFT).

Using (1–4) and the spheroid response given in [23], the ALLTEM response to the earth and the target are modeled separately, and then summed for the total response. Interactions between the target and surrounding medium are neglected (i.e., the Born approximation is used when calculating the response of the earth and the target individually). Figure 2 shows one cycle of the transmitter excitation, and the received response due to a non-permeable target ($\sigma = 10^7$ S/m) and to a permeable target ($\mu_r = 250$). A conductive non-permeable earth ($\sigma = 0.1$ S/m) was simulated in both cases. The earth response decays very rapidly and is not visible in Figure 2. The magneto-static response due to magnetization of a permeable target is manifest as a square wave response, with the decaying electro-dynamic response due to induced eddy currents superimposed. The square wave magneto-static response is absent for the non-permeable target. Note also that the electro-dynamic eddy current decay lasts longer for the permeable target. The bandwidth of the simulated data was limited to about 5 kHz (low-pass filter with a raised cosine taper and a 5 kHz-3 dB point), which is similar to the frequency response of the ALLTEM circuitry. This results in some ringing or oscillations in the simulations (and in the actual ALLTEM data) near the peaks of the transmitted

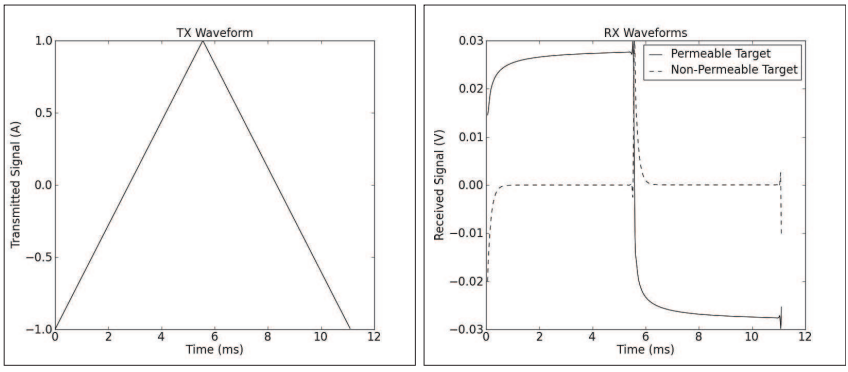

Figure 2. Left panel shows one cycle of the ALLTEM's transmitted waveform. Right panel contains received waveforms for permeable and non-permeable targets. Target is a 10 cm by 2 cm spheroid 50 cm deep with long axis in x-direction (see Figure 1). The VMD coil configuration shown in Figure 1 was used.

signal.

Although conductive soils do not adversely affect UXO surveys(most soils have a conductivity less than $1\,\mathrm{S/m}$), viscous magnetic soils do. To model the effects of viscous magnetic media, we use a continuous distribution of magnetic relaxation time constants [24],

$$\mu(\omega) = \mu_0 \left(1 + \chi(\omega)\right), \tag{5}$$

$$\chi(\omega) = \chi_{dc} \left(1 - \frac{1}{\ln(\tau_2/\tau_1)} \ln\left(\frac{i\omega\tau_2 + 1}{i\omega\tau_1 + 1}\right)\right), \tag{6}$$

where μ_0 is the permittivity of free space, is χ_{dc} is the magnetic susceptibility at zero frequency, and τ_1 and τ_2 are the lower and upper bounds of the continuous time constant distribution (taken as 10^{-6} and 10^{6} respectively for this work). This distribution is shown as a function of frequency in Figure 3, and fits the measured susceptibility of soil samples from Kaho'olawe, Hawaii [25]. Other distributions may be needed for soils in other locales. For example, Olhoeft and Strangway [26] used the Cole-Cole distribution to model frequency dependent magnetic properties of various eastern Canadian sulfide minerals. The Cole-Cole distribution is similar to the continuous distribution shown in Figure 3, however the band where the magnetic properties change with frequency is narrower in the Cole-Cole distribution. The difficulties presented by viscous magnetic soils are evident in Figure 3, where the response to the same target from Figure 2 is shown in viscous magnetic soil ($\chi_{dc} = 10^{-4}$ in MKS units). The characteristic shape of these curves is similar, making it difficult to

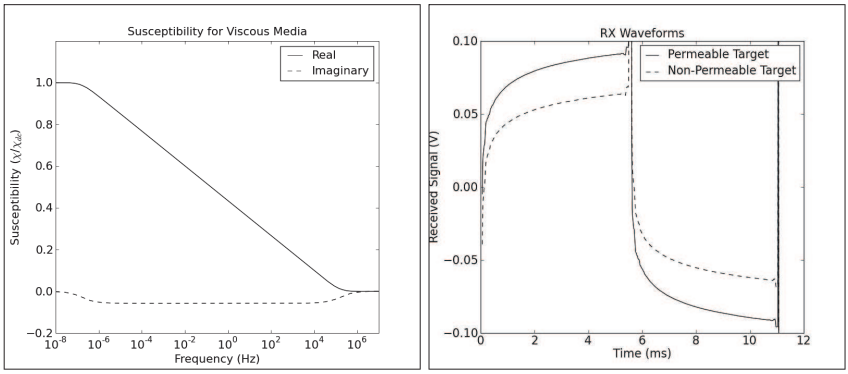

Figure 3. Left panel shows the modeled distribution of magnetic susceptibility versus frequency for viscous magnetic media. Right panel has the response to the same target modeled for Figure 2 in a viscous magnetic soil ($\chi_{dc} = 10^{-4}$ in MKS units).

distinguish between viscous magnetic soil and a magnetic target when making measurements from a single location (i.e., cued measurements). If the viscous magnetic effects have slow spatial variations, and have essentially the same values at locations surrounding the target, then background soil response can be subtracted from the target response before analyzing the target [19].

Calculating the Green's function in (1) and (4) is computationally expensive, and is not needed is most cases (i.e., when viscous magnetic soil is not present). A faster approach to calculating the magnetic fields is to use the static Biot-Savart Law for free space. This works especially well for the ALLTEM system since all coils have a square shape. The magnetic field at $\vec{r}$ is the sum of the fields produced by the four straight wire segments, each with current $\vec{I}_n$, length $2L$, and centered at $\vec{r}'_n$ (the midpoint of the wire segment):

$$\vec{H}(\vec{r}) = \sum_{n=1}^{4} \frac{\vec{I}_n \times \hat{R}_n}{4\pi} \left[\frac{\left|\vec{P}_n\right|}{d_2\left(d_2+L-\left|\vec{Z}_n\right|\right)} - \frac{\left|\vec{P}_n\right|}{d_1\left(d_1+L-\left|\vec{Z}_n\right|\right)} \right], \quad (7)$$

$$d_1 = \sqrt{L^2 + 2L\left|\vec{Z}_n\right| + \left|\vec{P}_n\right|^2 + \left|\vec{Z}_n\right|^2}, \quad (8)$$

$$d_2 = \sqrt{L^2 - 2L\left|\vec{Z}_n\right| + \left|\vec{P}_n\right|^2 + \left|\vec{Z}_n\right|^2}, \quad (9)$$

$$\vec{R}_n = \vec{r} - \vec{r}'_n, \quad (10)$$

$$\vec{Z}_n = \vec{R}_n \cdot \hat{I}_n, \quad (11)$$

$$\vec{P}_n = \vec{R}_n - \vec{Z}_n. \quad (12)$$

To calculate the target response, we avoid time-consuming spherical harmonic formulations [27] and begin with the simple parametric approximation presented by [28] for estimating the time-domain B field response of a conductive permeable sphere due to a step function excitation. This is also the electro-dynamic ALLTEM response since its excitation is integral of the step (i.e., a triangle wave), it uses dB/dt receivers, and the integral and derivative operations cancel each other. This parametric form is a good approximation to the early-time, intermediate-time, and late-time portions of the response. This simple form for permeable and non-permeable spheres reduces to:

$$M_{sphere}(t,R) = \frac{4\pi R^3}{3} \frac{9\mu_r}{2(\mu_r+2)} \left(1+\sqrt{\frac{t}{\alpha}}\right)^{-\beta} e^{-t/\gamma}, \quad (13)$$

$$\alpha = 1.38\tau_1, \quad (14)$$

$$\beta = \frac{2\sqrt{\alpha}\,(\mu_r+2)}{R\sqrt{\pi\sigma\mu_r\mu_0}}, \tag{15}$$

$$\gamma = \frac{\tau_0+\sqrt{\alpha\tau_0/2}}{1+\sqrt{\alpha/2\tau_0}-\beta/4}, \tag{16}$$

$$\tau_0 = \sigma\mu_r\mu_0 R^2/\delta_1^2, \tag{17}$$

$$\delta_1 = \pi+\arctan\left((\delta_1\mu_r-\delta_1)/\left(\mu_r-1+\delta_1^2\right)\right), \tag{18}$$

$$\tau_1^{\mu_r\approx 1} = \tau_0, \tag{19}$$

$$\tau_1^{\mu_r>>1} = \sigma\mu_r\mu_0 R^2/((\mu_r+2)(\mu_r-1)), \tag{20}$$

We combined this form with an approximation of the polarizability tensor for a spheroid in terms of that of a sphere [23]. For the nth element along the diagonal, this yields,

$$M_n(t) = \frac{2a^2b}{9R_n^3}\frac{\mu_r+2}{\mu_r}\left[\frac{1}{1-A_n}+\frac{\mu_r-1}{1+A_n(\mu_r-1)}\right]M_{sphere}(t,R_n), \tag{21}$$

$$R_1 = b, \tag{22}$$

$$R_2 = a, \tag{23}$$

where b is the half-length of the spheroid, a is the radius, and the demagnetization factors A_n are given in [23, eqns. A-2 and A-3]. The magneto-static response is simply

$$M_n^{DC} = \left[\frac{\mu_r-1}{1+A_n(\mu_r-1)}\right], \tag{24}$$

Combining both the electro-dynamic and the magneto-static responses, we obtain

$$M_n^{ALLTEM}(t) = 2M_n(t) - M_n(t=5.55\cdot 10^{-3}) - M_n^{DC}, \tag{25}$$

where the electro-dynamic response at 5.55 ms is subtracted to account for any eddy currents that have not fully decayed when the transmitted waveform changes slope. Ananalogous procedure may be used to obtain the polarizabilities for ellipsoids or non-ellipsoidal shapes [29, 30]. Finally, the time domain ALLTEM response is calculated from (26) and (27),

$$V_{rx}(t) = -\frac{\mu\vec{H}_{rx}(r)\cdot\overleftrightarrow{R}^T\cdot\overleftrightarrow{M}(t)\cdot\overleftrightarrow{R}\cdot\vec{H}_0(r)}{I_{rx}}, \tag{26}$$

where the diagonal components of $\overleftrightarrow{M}$ are from (25), $\vec{H}_0(r)$ is the primary magnetic field at the UXO location r due to the transmitter coil calculated using (7), $\vec{H}_{rx}(r)$ is the magnetic field at the UXO

location due to a test current (taken to be unity) in the receiver coil I_{rx} (also calculated using (7)), and it is assumed that the primary field is constant across the target. Since the ALLTEM uses two receiver coils in gradiometer configuration, the response is the difference between the two receiver signals,

$$\tilde{f}(\vec{x}) = V_{rx2}(t) - V_{rx1}(t). \tag{27}$$

3. INVERSION ALGORITHM

This section outlines a non-linear inversion routine developed for the ALLTEM instrument. The goal is to minimize the squared error between the modeled $\tilde{f}_j(\vec{x})$ and measured data f_j,

$$\min_{\vec{x}} \sum_{i}^{I \cdot J \cdot K} \left\| \tilde{f}_i\left(\vec{x}\right) - f_i \right\|^2, \tag{28}$$

where $\vec{x}$ contains the parameters, and the data index i iterates over the combinations of instrument locations I, coil combinations J, and time-gates K. The inversion employs an iterative Gauss-Newton minimization combined with step-size optimization as follows,

$$\vec{x}_{j+1} - \vec{x}_j = \alpha \left(\overleftrightarrow{J}^T \cdot \overleftrightarrow{J} \right)^{-1} \cdot \overleftrightarrow{J}^T (\vec{x}_j) \cdot \left(\vec{\tilde{f}}(\vec{x}_j) - \vec{f} \right), \tag{29}$$

$$J_{ij} = \frac{\partial}{\partial x_j} \tilde{f}_i\left(\vec{x}_j\right), \tag{30}$$

$$\min_{\alpha \in (0-1]} \left\| \vec{\tilde{f}}\left(\vec{x}_j\right) - \vec{f} \right\|^2. \tag{31}$$

Equation (29) is iterated until (28) is minimized. At each iteration j, the step length is scaled by α which is varied in discrete steps over the interval $(0, 1]$ to find the length that results in the smallest least squares data misfit. Since the number of data $(I \cdot J \cdot K)$ far exceeds the number of parameters to be estimated, (29) is calculated by singular value decomposition. Instabilities due to poor conditioning are avoided by scaling the parameters so their ranges all lie within 1–2 orders of magnitude, and by only using singular values that have magnitudes of at least 10^{-3} times the dominant singular value. At each iteration, the target's orientation angles are constrained to be between $-\pi$ and π, and the spheroid diameters are constrained to be positive. Iteration stops when a local minimum is found, or the maximum allowable number of iterations is reached. This basic search algorithm is used with a state machine to estimate the target parameters as described below.

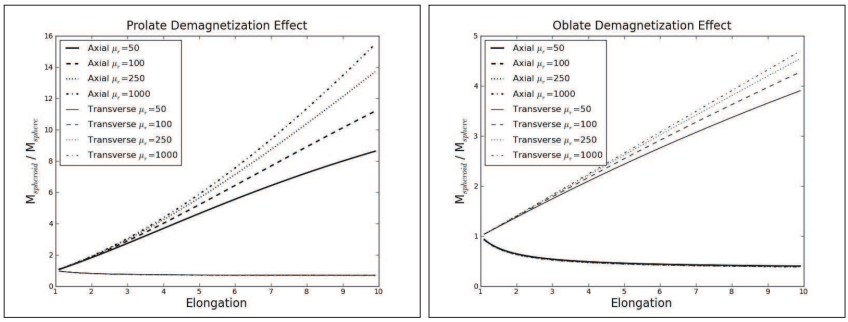

Figure 4. Left panel shows the demagnetization effect for prolate spheroids. Right panel shows demagnetization effect for oblate spheroids. Reduction in permeability due to saturation is not accounted for. $M_{\text{spheroid}}/M_{\text{sphere}}$ is the magnetization of a prolate spheroid along the principal axis normalized by that of a sphere.

The first step in the parameter estimation problem is to choose an initial model. The x and y target locations are selected from the centroid of the anomaly, and the initial z location is 0.5 m. To determine a representative permeability value, the late-time magnitudes are examined to determine if the target is ferrous or non-ferrous ($\mu_r = 1$). For ferrous targets, the demagnetization effect must be considered (see Figure 4). For targets with relative permeabilities ranging from 50 to 1000, a nominal value of 100 is sufficient to model objects with aspect ratios less than about four, therefore the selected representative value of μ_r is held fixed during the inversion. An initial conductivity is chosen based values of typical metals used in UXO construction. The conductivities of aluminum alloys typically range from about $1.5 \cdot 10^7$ to $3.5 \cdot 10^7$ S/m, and steel alloys typically range from $0.2 \cdot 10^7$ to $0.9 \cdot 10^7$ S/m, making $1.0 \cdot 10^7$ S/m a reasonable starting value. Initial orientation angles (pitch and yaw) are zero.

Determining reasonable initial spheroid diameters is more difficult. With a representative permeability value, it is possible to determine the principal spheroid diameters using the response at time $t = 0^+$ (the instant the transmitter turns off). This however, requires a system with instantaneous turn-off time and a receiver with infinite bandwidth. With some high-bandwidth systems, it may be possible to extrapolate back from earliest available time sample at a slope of $t^{1/2}$ to estimate the dimensions of the target. Equations (13)–(24) illustrate that the very early time amplitude is a function only of permeability, size, and shape; and that the rest of the curve is a

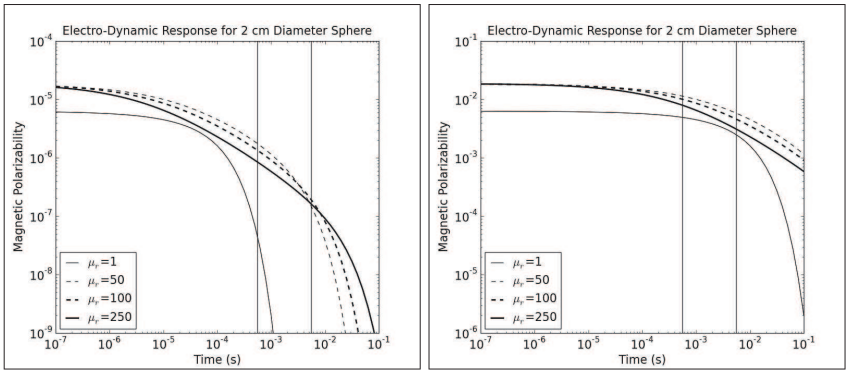

Figure 5. Electro-dynamic decay curves for permeable and non-permeable spheres with different sizes. The vertical lines bracket the time interval where ALLTEM data are available.

function the response parameters τ_n (i.e., conductivity, permeability, size, and shape). For permeable targets, the change in rate of decay from early time (decaying at $t^{-1/2}$) to intermediate-time (decaying at $t^{-\beta/2}$) occurs at time $t = \tau_1$; and the change to late-time (decaying at $e^{-t/\gamma}$) occurs at $t = \tau_0$. If attributes τ_0 and τ_1 could be reliably picked from the decay curve, then the independent equations for these attributes could be used to estimate both permeability and radius. For non-permeable targets, the change in rate of decay from early time (decaying at $t^{-1/2}$) to late-time (decaying at $e^{-t/\gamma}$) occurs at time $t = \tau_0$. These concepts are illustrated in Figure 5, which shows the decay curves for permeable and non-permeable spheres with different sizes.

The data used in this study were recorded by the USGS at the Denver Federal Center, where a test stand was built to measure the response of known UXO targets [31]. There is a large amount of ambient EM noise at the Denver Federal Center where high amplitude VLF emissions and other noise sources exist. Subsequently, the supplied data had been heavily median filtered to suppress very low frequency (VLF) noise (see Figure 6). This resulted in distorted amplitudes in early-time data, making analysis at times less than about 500 µs impractical. Estimating principal spheroid diameters using early times with ALLTEM is not possible due to the heavy median filtering and the limited bandwidth (∼5 kHz) of the system.

In conducting trials with the minimization algorithm, it was observed that there is a basin of attraction associated with both

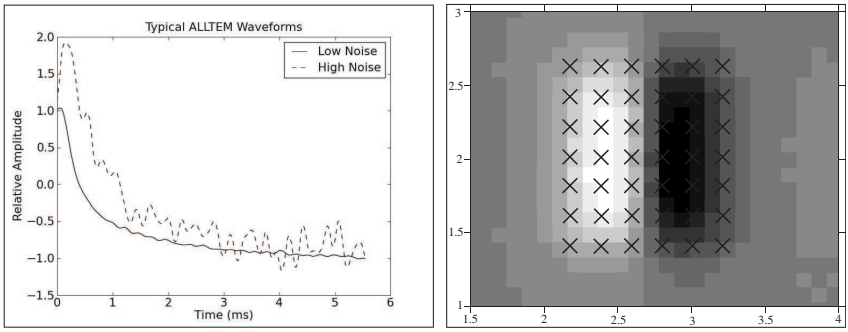

Figure 6. Left panel shows typical ALLTEM test stand data after heavy median filtering. Noise is primarily due to VLF stations near the test bed. A high-noise and a low-noise decay curve are shown, with both curves normalized to their initial value. Right panel shows the plan view of a typical anomaly for single coil combination (xzm over an 81 mm target, see Appendix B). Black Xs indicate plan-view instrument locations where data are taken for analysis.

prolate models and oblate models. Oftentimes, the evolving data misfit function would enter an incorrect basin of attraction only to find a local minimum. The solution to this problem is to minimize the misfit function using a prolate model, then using an oblate model, and then choose the solution with the best fit. In this work, both initial models use a larger diameter of 0.26 m and a smaller diameter of 0.1 m.

The mean squared error in the best-fit modeled data is assumed to be due to variations from a non-ideal systematic response. These variations include components of the instrument response not accounted for by the model (drift, non-linear response, etc.), components of target response not accounted for by the model, ambient EM noise, geologic noise, errors in instrument location, and attitude variations of the instrument. To estimate the uncertainty in the estimated parameters, each parameter is perturbed from its best-fit value until the mean squared error of the modeled data increases by the noise variance estimate from the data. To estimate the noise variance, the deviation of the data from a line drawn between time samples $t = 4.5$ and 5.5 ms is used for each waveform. Thus, the uncertainty calculations only account for data noise measured by the noise variance estimator, and may not reflect components that are not measured such as instrument drift.

The number of data points is typically chosen to be less than $\sim$1000 so that the inversion can be accomplished in a reasonable time

frame (about a minute using a PC with a 2 GHz 32-bit processor). When selecting a set of coil combinations to use in the analysis, the set that carries the most (orthogonal) information is desirable. To select a subset of coil combinations from the recorded set of 19 coil combinations, selections are made in order of increasing noise variance until a single selection for each of the nine possible polarization combinations (i.e., (Tx_x, Rx_x), (Tx_x, Rx_y), etc.) has been made. If more coil combinations are needed to fill the subset, then additional selections are made in order of increasing noise variance. Although several time-gates can be used, only data from a single time-gate (typically at $t = 5$ ms) are typically used for numerical efficiency. Because most of the energy in the ALLTEM waveforms from ferrous targets at times greater than 1 ms is magneto-static, the μ and σ are held fixed to reduce the degrees of freedom while searching for optimum prolate and oblate models. The final (optional) step is to refine the estimated conductivity value using the best solution found thus far, using multiple (typically 5) time-gates and holding all other parameters fixed.

4. INVERSION PERFORMANCE

In this section, we examine the benefits of having more coil combinations and more spatial locations; and the detrimental effects

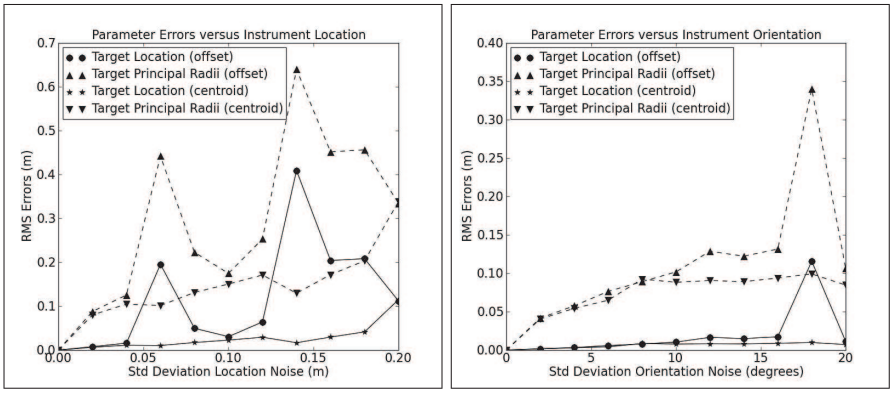

Figure 7. Left panel shows effects of instrument location errors, and the right panel shows the effects of instrument orientation errors. The principal lengths are most sensitive to location and orientation errors. Nine coil combinations were used. There was no noise added to the simulated waveforms so that errors could be attributed to instrument location and orientation.

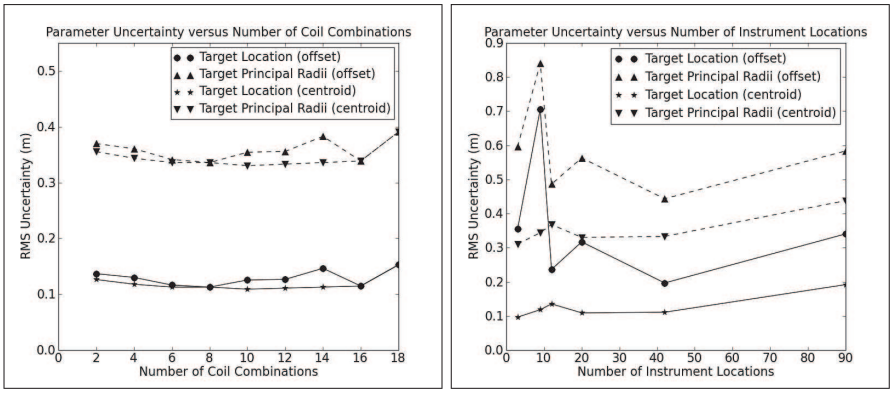

Figure 8. Left panel shows the reduction of uncertainty as more coil combinations are used. Right panel shows the reduction of uncertainty as more spatial locations are used. The spatial locations were distributed over grids with the following dimensions: (1×3), (3×3), (3×4), (4×5), (6×7), and (9×10). All grids spanned a $1.44\,\mathrm{m}^2$ except the (1x3) arrangement, which was 3 points in a line spanning 1.2 m.Nine coil combinations were used. In both cases, the synthetic waveforms had normally distributed noise added ($\sigma_{\mathrm{sd}} = 5\,\mathrm{mV}$ with a 20 amp excitation, SNR$\approx$10 : 1) to simulate a more realistic situation.

of uncertain cart orientation, position error, and noise in the data. We begin by synthesizing a data set for a prolate spheroid with diameters of 60 by 140 mm at a depth of 245 mm, with the long axis in the horizontal plane. Data were modeled for 42 instrument locations uniformly distributed over a square area of $1.44\,\mathrm{m}^2$ centered over the target (see Figure 6); and five time samples (1–5 ms) were simulated at each instrument location. Figure 7 shows the RMS errors of the estimated target position and spheroid principal length versus errors in the instrument location (i.e., simulated GPS uncertainties) and orientation (i.e., simulated cart tilt due to surface roughness). In each case, random (normally distributed) position and orientation errors were added at each instrument location. For inversion, the data from the nine coil combinations with the smallest noise variance were selected to make a dataset of all nine polarization combinations (i.e., ($\mathrm{Tx_x}$, $\mathrm{Rx_x}$), ($\mathrm{Tx_x}$, $\mathrm{Rx_y}$), etc.). These results demonstrate that significant errors ($>\sim 10\,\mathrm{cm}$) in the estimated principal radii of spheroid occur when errors in location and orientation increase beyond 3 cm and 10 degrees respectively. Barrow and Nelson [32] found similar results due to errors in height.

The effect of the number of coils combinations and spatial samples was also investigated, and the results are shown in Figure 8. Initially, using more coil combinations reduces the RMS uncertainty in the estimated target parameters. When more than about nine coil combinations are used, the uncertainty plateaus or may increase. Because low noise variance coil combinations are selected first, one may conclude that adding coil combinations with large noise variance does not help to further constrain the solution. Adding more instrument locations does not appreciably reduce parameter uncertainties, but is does reduce appear to reduce the markedly different results obtained from different starting models.

Noise in the measured waveforms, position, or orientation can cause more local minimums to appear in the objective function used to invert the data. The ramifications of this are different inversion results from different starting models. Inversion results from two different starting model locations are shown in Figures 7 and 8: one based on the data centroid (described above), and the other offset from the true location by 0.1 m in the x, y, and z directions. The errors and uncertainties resulting from different starting models are similar in many cases, indicating that the inversion is finding solutions near the global minimum. On other cases, the differences are quite large, indicating that noise can trap the inversion in a local minimum far from the global solution. These difficulties could be reduced by smoothing the objective function or by using a suitable optimization algorithm such as simulated annealing or a genetic algorithm.

Table 1. Inversion results for the steel sphere. 14 coil combinations were used. True values are listed in the first column. Lengths are in m, and angles are in degrees. M.S. = magneto-static; E.D. = electro-dynamic.

Steel Sphere (reference values)	$t = 5$ ms (M.S) ($\sigma_{\text{noise}} = 4.4\%$ MSE = 2.8)	$t = 3$ ms (E.D.) ($\sigma_{\text{noise}} = 35\%$ MSE = 14%)	$t = 2$ ms (E.D) ($\sigma_{\text{noise}} = 19\%$ MSE = 3.7%)	$t = 1$ ms (E.D.) ($\sigma_{\text{noise}} = 9.2\%$ MSE = 1.2%)
x (2.066)	2.057 ($\pm$0.130)	2.054 ($\pm$0.425)	2.053 ($\pm$0.285)	2.055 ($\pm$0.190)
y (2.667)	2.685 ($\pm$0.165)	2.639 ($\pm$0.515)	2.656 ($\pm$0.340)	2.658 ($\pm$0.230)
z (0.499)	0.515 ($\pm$0.050)	0.476 ($\pm$0.220)	0.501 ($\pm$0.125)	0.511 ($\pm$0.080)
Length (0.05)	0.055 ($\pm$0.018)	0.037 ($\pm$0.021)	0.042 ($\pm$0.017)	0.046 ($\pm$0.014)
Width (0.05)	0.053 ($\pm$0.008)	0.037 ($\pm$0.010)	0.042 ($\pm$0.008)	0.046 ($\pm$0.006)

Table 2. Inversion results for a 60 mm ordinance (U.S. PROJECTILE, 60-MM, HE, M49A4), which has a steel body and tail. 14 coil combinations were used. True values are listed in the first column. Lengths are in m, and angles are in degrees. M.S. = magneto-static; E.D. = electro-dynamic.

60 mm ordnance	$t = 5$ ms (M.S.) ($\sigma_{\text{noise}} = 1.7\%$ MSE = 0.56%)	$t = 3$ ms (E.D.) ($\sigma_{\text{noise}} = 12.6\%$ MSE = 2.4%)	$t = 2$ ms (E.D.) ($\sigma_{\text{noise}} = 6.6\%$ MSE = 1.7%)	$t = 1$ ms (E.D.) ($\sigma_{\text{noise}} = 3.3\%$ MSE = 0.86%)
x (2.066)	2.091 ($\pm$0.055)	2.085 ($\pm$0.175)	2.085 ($\pm$0.120)	2.086 ($\pm$0.080)
y (2.667)	2.663 ($\pm$0.095)	2.672 ($\pm$0.085)	2.670 ($\pm$0.065)	2.667 ($\pm$0.060)
z (0.245)	0.262 ($\pm$0.025)	0.295 ($\pm$0.075)	0.294 ($\pm$0.050)	0.266 ($\pm$0.030)
Length (0.117)	0.098 ($\pm$0.011)	0.087 ($\pm$0.010)	0.096 ($\pm$0.010)	0.094 ($\pm$0.007)
Width (0.030)	0.032 ($\pm$0.005)	0.020 ($\pm$0.014)	0.022 ($\pm$0.011)	0.025 ($\pm$0.007)
Azimuth (0.0)	0.407 ($\pm$7.44)	0.195 ($\pm$6.88)	0.511 ($\pm$5.16)	0.579 ($\pm$5.73)
Inclin. (0.0)	0.452 ($\pm$12.6)	-0.447 ($\pm$13.8)	-0.589 ($\pm$9.74)	-0.564 ($\pm$9.74)

Next, we analyze inversion results obtained from ALLTEM data collected by the USGS over known targets. For targets comprised of both ferrous and non-ferrous metals, [33] discuss using data at each time-gate separately so that different locations of the induced dipole moments can be determined, but do not present any data to illustrate the concept. The goal is to leverage the fact that eddy currents should persist for longer times in ferrous portions of the target than in non-ferrous portions to provide better diagnostic information. One could reason that adding magneto-static information to the dataset may provide even more information about the distribution of different metals in the target. Tables 1–3 show inversion results for different targets and time-gates. The targets were a steel ball, a 60 mm target (U.S. Projectile, 60-mm, HE, M49A4) that is entirely made from steel, and an 81 mm target (U.S. Projectile HE, M889A1) that has a steel body and an aluminum tail. When analyzing electro-dynamic datasets (i.e., data from early time-gates), the DC term in (21) is removed from the forward model and the data value at 5.55 ms was subtracted from the measured waveform. When analyzing magneto-static datasets, only the 5 ms time-gate is used to estimate target location and shape. In this case, the response is essentially magneto-static. In general,

results obtained from the late-time magneto-static response are similar to those obtained from early-time data. The uncertainty of target parameter estimates is less when using earlier time-gates because the signal to noise ratio is larger (smaller noise variance). No significant movement of target location versus time is observed in the results from the 81 mm target.

Finally, a synthetic dataset was created for a compound target. The compound target response was modeled by superposing (it was assumed that superposition would provide reasonable accuracy) the response of two horizontal prolate spheroids with diameters of 60 by 140 mm at a depth of 245 mm, one ferrous and the other non-ferrous. The spheroids were co-located except that they were offset by 10 cm along their major axis. Inversions results are shown in Table 4. Target locations determined using magneto-static data reflect the location of the ferrous spheroid, while those from electro-dynamic data reflect the location of the composite body. Very little movement of the target location is seen for different time-gates. This is likely due to the large amplitude and decay time of ferrous targets compared to those of non-ferrous targets.

Since a non-ferrous object does not have a magneto-static

Table 3. Inversion results for an 81 mm ordinance (U.S. Projectile, 81-mm, HE, M889A1), which has a steel body and an aluminum tail. 14 coil combinations were used.True values are listed in the first column. Lengths are in m, and angles are in degrees. M.S.= magneto-static; E.D.= electro-dynamic.

81 mm Ordnance	$t = 5$ ms (M.S.) ($\sigma_{\text{noise}} = 1.1\%$ MSE = 2.3)	$t = 3$ ms (E.D.) ($\sigma_{\text{noise}} = 8.2\%$ MSE = 4.1)	$t = 2$ ms (E.D.) ($\sigma_{\text{noise}} = 4.0\%$ MSE = 3.4)	$t = 1$ ms (E.D.) ($\sigma_{\text{noise}} = 1.8\%$ MSE = 2.9)
x(2.066)	2.048 ($\pm$0.045)	2.062 ($\pm$0.120)	2.058 ($\pm$0.085)	2.060 ($\pm$0.055)
y (2.667)	2.666 ($\pm$0.095)	2.662 ($\pm$0.115)	2.664 ($\pm$0.090)	2.665 ($\pm$0.075)
z (0.245)	0.269 ($\pm$0.020)	0.300 ($\pm$0.055)	0.296 ($\pm$0.035)	0.290 ($\pm$0.025)
Length (0.215)	0.116 ($\pm$0.012)	0.091 ($\pm$0.012)	0.101 ($\pm$0.010)	0.108 ($\pm$0.009)
Width (0.041)	0.045 ($\pm$0.006)	0.029 ($\pm$0.011)	0.034 ($\pm$0.008)	0.040 ($\pm$0.006)
Azimuth (0.0)	1.18 ($\pm$8.02)	$-$0.004 ($\pm$9.17)	0.511 ($\pm$6.88)	0.398 ($\pm$6.30)
Inclin. (0.0)	0.96 ($\pm$12.0)	$-$0.230 ($\pm$15.5)	$-$0.329($\pm$11.5)	$-$1.18 ($\pm$9.74)

Table 4. Inversion results for modeled compound target made from two spheroids, one ferrous and the other non-ferrous. True values are listed in the first row. Lengths are in m. M.S. = magneto-static; E.D. = electro-dynamic.

Compound Target	x (2.015 non-ferrous, 2.115 ferrous)	y (2.667)	z (0.245)
$t = 0.3$ ms (E.D.)	2.085	2.667	0.248
$t = 0.5$ ms (E.D.)	2.085	2.667	0.248
$t = 1$ ms (E.D.)	2.086	2.667	0.248
$t = 2$ ms (E.D.)	2.087	2.667	0.249
$t = 3$ ms (E.D.)	2.088	2.667	0.250
$t = 5$ ms (M.S.)	2.119	2.667	0.244

response, discriminating between ferrous and non-ferrous objects is trivial with the ALLTEM system — non-ferrous targets have a nearly zero late-time response. This discrimination is certainly possible using only the electro-dynamic response as measured by conventional TDEM systems. However this may require multiple time-gates, will add another parameter for the inversion to estimate (μ_r), and may be difficult with noisy data. Note that the benefits of making on-time measurements come with the well-known difficulties of building an instrument with a stable response.

5. CONCLUSIONS

A fully polarimetric instrument such as the ALLTEM that makes both a magneto-static and an electro-dynamic excitation provides a rich dataset. A frequency-domain model of the ALLTEM response was created that accounts for both the target and the ground response. A faster time-domain model was created that only accounts for the target response, and an inversion algorithm was built using this model. We have analyzed synthetic and actual ALLTEM data with an inversion algorithm that makes use of multiple instrument locations, multiple coil combinations, magneto-static, and electro-dynamic data. From this work, the following conclusions are made.

1. Although either electro-dynamic or the magneto-static excitation provides enough data to independently estimate metallic target parameters, discrimination between ferrous and non-ferrous targets is easier when both the responses are measured.
2. Analysis of modeled and actual data shows that it is possible to observe different induced dipole moments locations for the

magneto-static and the electro-dynamic response in targets that are constructed with multiple types of metal.

3. For the scenarios examined in this paper, the minimum ALLTEM datasets that provided acceptable inversion results have at least four coil combinations, and at least 12 instrument locations arranged in a 3×3 grid covering $1.44\,\mathrm{m}^2$. These results are only valid for the target parameters tested. Different results are likely for targets with different size, aspect ratio, and depth.
4. When a sufficient number of coil combinations are used, this problem is not ill-posed and is over-determined. However, non-linearities and uncertainties in array position and orientation result in multiple local minima that make it more difficult to find the global minimum. Adding more instrument locations does not appreciably reduce parameter uncertainties, but it does reduce appear to reduce the occurrence of local minima. Smoothing in the objective function by regularization or a-priori knowledge to eliminate local minima would be more efficient than adding more data.
5. Significant errors ($>\sim 10\,\mathrm{cm}$) in the estimated principal length and location of the target occur when errors in location and orientation increase beyond 3 cm and 10 degrees respectively. Again, these results are only valid for the target parameters tested. Different results are likely for targets with different size, aspect ratio, and depth.
6. Constraining the model to a spheroid and inverting for spheroid axis lengths provides more intuitive target characteristics than the eigen values of the induced polarizabilty tensor (i.e., principal polarizabilities) because demagnetization and volumetric effects are accounted for. More descriptive target parameterizations may provide better input to library based classification algorithms. The spheroid radii estimates are more intuitive than principal polarizabilties and magnetic surface charge distributions [34], but may not provide as much information to a classification algorithm as the latter method.
7. The transient electro-dynamic response of the soil decays very quickly ($O(100\,\mu\mathrm{s})$ for $\sigma = 1\,\mathrm{S/m}$) and does not affect the measured ALLTEM target response. Viscous magnetic soils do however have a pronounced effect that interferes with the target response. Results show that viscous magnetic soils with $\chi_{dc} = 10^{-4}$ in MKS units produce nearly the same signal as a $10 \times 2\,\mathrm{cm}$ prolate spheroid. Viscous magnetic soils with permeabilities greater than 10^{-6} MKS units cause detrimental interference to the

response to targets with volumes on the order of 40 cm^3. In cases where the spatial variation of magnetic soil properties is low (i.e., large correlation lengths), subtracting the regional background response may facilitate proper target analysis [35].

8. For the electro-dynamic response, using a triangle wave excitation with dB/dt receivers is equivalent to using a square wave excitation with B field receivers. This configuration provides a slower decay than a square wave excitation with dB/dt field receivers, which enhances late-time measurements [28]. It also enables the use of receivers with less dynamic range. The decaying response of a 20 mm sphere from 0 to 40 ms spans 3.5 orders of magnitude with a triangle excitation and dB/dt receivers, and spans 7.2 orders of magnitude with a square wave excitation.

Future work should investigate the ability to discriminate between hollow and solid metallic targets, and attempt to determine the thickness of the outer shell. Analysis routines should be able to determine when an anomaly is due to multiple targets in close proximity with overlapping responses, and inversion routines should be able to handle the overlapping responses of multiple targets. An inversion that models an ellipsoid or other target shapes [29, 30] rather than a spheroid may provide better UXO characterization. This paper analyzed datasets acquired from stationary instrument locations over a few different types of targets. Future work should account for and compensate for positional and orientational uncertainties, and compare the accuracy of results taken from both stationary measurements and moving measurements. We intend to publish results from field surveys for a wide variety of targets elsewhere.

ACKNOWLEDGMENT

We are grateful to Ted Asch and Craig Moulton at the U.S. Geological Survey for supplying a complete set of ALLTEM data collected for known UXO targets. These data were acquired using a custom built test stand that was designed to remove any effects of soil. Additionally, D. (Skip) Snyder, and Dave George provided valuable information regarding the MetalMapper instrument. Yaoguo Li and MisacNabighian also provided useful discussions.

APPENDIX A.

Ward and Hohmann [20] and Parise [21] derive the following expressions for the magnetic fields on or above a half-space due to

a magnetic dipole on or above a half-space. These expressions are combined to form the dyadic Green's function as follows. Note that the origin is at the surface with the z-axis positive down. Material properties have subscript 0 for air, and 1 for earth.

$$\overleftrightarrow{G}^{-}(x,y,z,x',y',z') = \frac{m}{4\pi}\begin{bmatrix} g_{11}^{-} & g_{12}^{-} & g_{13}^{-} \\ g_{21}^{-} & g_{22}^{-} & g_{23}^{-} \\ g_{31}^{-} & g_{32}^{-} & g_{33}^{-} \end{bmatrix} \tag{A1}$$

$$g_{11}^{-} = -\left(\frac{1}{\bar{\rho}} - \frac{2\bar{x}^2}{\bar{\rho}^3}\right)\int_0^{\infty}\left[e^{-ik_{0z}(z-z')} - r_{te}e^{ik_{0z}(z+z')}\right]\lambda J_1(\lambda\bar{\rho})d\lambda$$
$$-\frac{\bar{x}^2}{\bar{\rho}^3}\int_0^{\infty}\left[e^{-ik_{0z}(z-z')} - r_{te}e^{ik_{0z}(z+z')}\right]\lambda^2 J_0(\lambda\bar{\rho})d\lambda \tag{A2}$$

$$g_{21}^{-} = g_{12}^{-} = \frac{\bar{x}\bar{y}}{\bar{\rho}^3}\int_0^{\infty}\left[e^{-ik_{0z}(z-z')} - r_{te}e^{ik_{0z}(z+z')}\right]\lambda J_1(\lambda\bar{\rho})d\lambda$$
$$-\frac{\bar{x}\bar{y}}{\bar{\rho}^2}\int_0^{\infty}\left[e^{-ik_{0z}(z-z')} - r_{te}e^{ik_{0z}(z\_z')}\right]\lambda^2 J_0(\lambda\bar{\rho})d\lambda \tag{A3}$$

$$g_{31}^{-} = g_{13}^{-} = \frac{\bar{x}}{\bar{\rho}}\int_0^{\infty}\left[e^{-ik_{0z}(z-z')} + r_{te}e^{ik_{0z}(z+z')}\right]\lambda^2 J_1(\lambda\bar{\rho})d\lambda \tag{A4}$$

$$g_{22}^{-} = -\left(\frac{1}{\bar{\rho}} - \frac{2\bar{y}^2}{\bar{\rho}^3}\right)\int_0^{\infty}\left[e^{-ik_{0z}(z-z')} - r_{te}e^{ik_{0z}(z+z')}\right]\lambda J_1(\lambda\bar{\rho})d\lambda$$
$$-\frac{\bar{y}^2}{\bar{\rho}^3}\int_0^{\infty}\left[e^{-ik_{0z}(z-z')} - r_{te}e^{ik_{0z}(z+z')}\right]\lambda^2 J_0(\lambda\bar{\rho})d\lambda \tag{A5}$$

$$g_{32}^{-} = g_{23}^{-} = \frac{\bar{y}}{\bar{\rho}}\int_0^{\infty}\left[e^{-ik_{0z}(z-z')} + r_{te}e^{ik_{0z}(z+z')}\right]\lambda^2 J_1(\lambda\bar{\rho})d\lambda \tag{A6}$$

$$g_{33}^{-} = \int_0^{\infty}\left[e^{-ik_{0z}(z-z')} + r_{te}e^{ik_{0z}(z+z')}\right]\frac{\lambda^3}{ik_z}J_0(\lambda\bar{\rho})d\lambda \tag{A7}$$

$$\bar{x} = x - x' \tag{A8}$$

$$\bar{y} = y - y' \tag{A9}$$

$$\bar{\rho} = \sqrt{(x-x')^2 + (y-y')^2} \tag{A10}$$

$$k_{nz} = \sqrt{k_n^2 - \lambda^2} \tag{A11}$$

$$k_n = \sqrt{-i\omega\mu_n\sigma_n + \omega^2\mu_n\varepsilon_n} \tag{A12}$$

$$r_{te} = \frac{\mu_1 k_{0z} - \mu_0 k_{1z}}{\mu_1 k_{0z} + \mu_0 k_{1z}} \tag{A13}$$

Here, m is the dipole moment, r_{te} is the transverse-electric plane-wave reflection coefficient, and k_{nz} is the wave number for medium n. With a similar analysis, we arrive at the Green's tensors for fields below the

surface for a dipole on or above the surface.

$$\overleftrightarrow{G}^{+}(x,y,z,x',y',z') = \frac{m}{4\pi}\begin{bmatrix} g_{11}^{+} & g_{12}^{+} & g_{13}^{+} \\ g_{21}^{+} & g_{22}^{+} & g_{23}^{+} \\ g_{31}^{+} & g_{32}^{+} & g_{33}^{+} \end{bmatrix} \tag{A14}$$

$$g_{11}^{+} = -\frac{\mu_0}{\mu_1}\left(\frac{1}{\bar{\rho}} - \frac{2\bar{x}^2}{\bar{\rho}^3}\right)\int_0^\infty e^{ik_{0z}z'}t_{te}e^{-ik_{1z}z}ik_{1z}J_1(\lambda\bar{\rho})d\lambda$$
$$-\frac{\mu_0}{\mu_1}\frac{\bar{x}^2}{\bar{\rho}^3}\int_0^\infty e^{ik_{0z}z'}t_{te}e^{-ik_{1z}z}ik_{1z}\lambda J_0(\lambda\bar{\rho})d\lambda \tag{A15}$$

$$g_{21}^{+} = g_{12}^{+} = -\frac{\mu_0}{\mu_1}\frac{\bar{x}\bar{y}}{\bar{\rho}^3}\int_0^\infty e^{ik_{0z}z'}t_{te}e^{-ik_{1z}z}ik_{1z}J_1(\lambda\bar{\rho})d\lambda$$
$$-\frac{\mu_0}{\mu_1}\frac{\bar{x}\bar{y}}{\bar{\rho}^2}\int_0^\infty e^{ik_{0z}z'}t_{te}e^{-ik_{1z}z}ik_{1z}\lambda J_0(\lambda\bar{\rho})d\lambda \tag{A16}$$

$$g_{31}^{+} = g_{13}^{+} = \frac{\mu_0}{\mu_1}\frac{\bar{x}}{\bar{\rho}}\int_0^\infty e^{ik_{0z}z'}t_{te}e^{-ik_{1z}z}\frac{k_{1z}\lambda^2}{k_{0z}}J_1(\lambda\bar{\rho})d\lambda \tag{A17}$$

$$g_{22}^{+} = -\frac{\mu_0}{\mu_1}\left(\frac{1}{\bar{\rho}} - \frac{2\bar{y}^2}{\bar{\rho}^3}\right)\int_0^\infty e^{ik_{0z}z'}t_{te}e^{-ik_{1z}z}ik_{1z}J_1(\lambda\bar{\rho})d\lambda$$
$$-\frac{\mu_0}{\mu_1}\frac{\bar{y}^2}{\bar{\rho}^3}\int_0^\infty e^{ik_{0z}z'}t_{te}e^{-ik_{1z}z}ik_{1z}\lambda J_0(\lambda\bar{\rho})d\lambda \tag{A18}$$

$$g_{32}^{+} = g_{23}^{+} = \frac{\mu_0}{\mu_1}\frac{\bar{y}}{\bar{\rho}}\int_0^\infty e^{ik_{0z}z'}t_{te}e^{-ik_{1z}z}\frac{k_{1z}\lambda^2}{k_{0z}}J_1(\lambda\bar{\rho})d\lambda \tag{A19}$$

$$g_{33}^{+} = \frac{\mu_0}{\mu_1}\int_0^\infty e^{ik_{0z}z'}t_{te}e^{-ik_{1z}z}\frac{\lambda^3}{ik_{0z}}J_0(\lambda\bar{\rho})d\lambda \tag{A20}$$

$$t_{te} = \frac{2\mu_1 k_{0z}}{\mu_1 k_{0z} + \mu_0 k_{1z}} \tag{A21}$$

APPENDIX B.

All of the coils on the ALLTEM system are located on a one-meter cube (see Figure 1). The size, location, and orientation of the coil combinations are defined by a three-character mnemonic. The first two letters refer to the polarization of the transmitter and receiver coils respectively. All three transmitter coils are one meter square, and are centered on the cube. The last character refers to the location and size of the receiver gradiometer coil pair. The size of the receiver coils, the midpoint between the receiver coils, and the offset from the midpoint to each coil is listed in Table B1. Midpoints are measured from the center of the cube.

Table B1. ALLTEM coil parameters. All dimensions in meters. Coil mnemonics are listed in order of decreasing amplitude for a steel ball target.

Mnemonic	Coil side length	Midpoint (x, y, z)	Offset (x, y, z)
zzm	1.0	(0.0, 0.0, 0.0)	(0.0, 0.0, +/ − 0.5)
xzm	1.0	(0.0, 0.0, 0.0)	(0.0, 0.0, +/ − 0.5)
yzm	1.0	(0.0, 0.0, 0.0)	(0.0, 0.0, +/ − 0.5)
zzh	0.35	(0.0, 0.0, 0.0)	(0.25, −0.25, +/ − 0.5)
xze	0.35	(0.0, 0.0, 0.0)	(0.25, 0.25, +/ − 0.5)
yze	0.35	(0.0, 0.0, 0.0)	(0.25, 0.25, +/ − 0.5)
zze	0.35	(0.0, 0.0, 0.0)	(0.25, 0.25, +/ − 0.5)
xx1	0.35	(0.0, 0.0, 0.292)	(+/ − 0.5, 0.0, 0.0)
yy1	0.35	(0.0, 0.0, 0.292)	(0.0, +/ − 0.5, 0.0)
xzf	0.35	(0.0, 0.0, 0.0)	(−0.25, 0.25, +/ − 0.5)
yzg	0.35	(0.0, 0.0, 0.0)	(−0.25, -0.25, +/ − 0.5)
yzf	0.35	(0.0, 0.0, 0.0)	(−0.25, 0.25, +/ − 0.5)
yzh	0.35	(0.0, 0.0, 0.0)	(0.25, −0.25, +/ − 0.5)
zzf	0.35	(0.0, 0.0, 0.0)	(−0.25, 0.25, +/ − 0.5)
zzg	0.35	(0.0, 0.0, 0.0)	(−0.25, −0.25, +/ − 0.5)
xzg	0.35	(0.0, 0.0, 0.0)	(−0.25, −0.25, +/ − 0.5)
xzh	0.35	(0.0, 0.0, 0.0)	(0.25, −0.25, +/ − 0.5)
zx1	0.35	(0.0, 0.0, 0.292)	(+/ − 0.5, 0.0, 0.0)
zy1	0.35	(0.0, 0.0, 0.292)	(0.0, +/ − 0.5, 0.0)

REFERENCES

1. McNeill, J. D. and M. Bosnar, "Applications of TDEM techniques to metal detection and discrimination: A case history with the new geonics EM-63 fully time-domain metal detector," AN-32, Geonics, Mississauga, ON, Canada, 2000.
2. Won, I. J., D. Keiswetter, and T. H. Bell, "Electromagnetic induction spectroscopy for clearing landmines," *IEEE Trans. Geoscience and Remote Sensing*, Vol. 39, No. 4, 703–709, 2001.
3. Mahmoudi, M. and S. Y. Tan, "Depth detection of conducting marine mines via eddy-current and current-channeling response," *Progress In Electromagnetics Research*, Vol. 90, 287–307, 2009.
4. Huang, H. and I. J. Won, "Detecting metal objects in magnetic environments using a broadband electromagnetic method," *Geophysics*, Vol. 68, No. 6, 1877–1887, 2003.
5. Pasion, L. R., "Inversion of time domain electromagnetic data for the detection of unexploded ordinance," Ph.D. Thesis, U. of

British Columbia, Vancouver, BC, Canada, 2007.

6. Morrison, F., T. Smith, A. Becker, and E. Gasperikova, "Detection and classification of buried metal objects," Final Report, UX-1225, Paper LBNL-53962, Lawrence Berkeley National Laboratory, Berkeley, CA, 2005.
7. Baum, C. E., "Detection and identification of visually obscured targets," Taylor and Francis, Philadelphia, PA, 1999.
8. Wright, D. L., C. W. Moulton, T. H. Asch, S. R. Hutton, P. J. Brown, M. N. Nabighian, and Y. Li, "ALLTEM, a triangle wave on-time time-domain system for UXO applications," *Symp. on the Application of Geophysics to Engineering & Environmental Problems*, Vol. 18, 1357–1367, Environmental and Engineering Geophysical Society, Denver, CO, 2005.
9. Gasperikova, E., J. T. Smith, H. F. Morrison, and A. Becker, "Berkeley UXO discriminator (BUD)," Lawrence Berkeley National Lab, Paper LBNL-62263, 2007.
10. Pasion, L. R., S. D. Billings, K. A. Kingdon, D. W. Oldenburg, N. Lhomme, and J. Jacobson, "Cooperative inversion of time domain electromagnetic and magnetometer data for the discrimination of unexploded ordnance," *J. Env. and Eng. Geoph.*, Vol. 13., No. 3, 193–210, 2008.
11. Oden, C. P. and C. W. Moulton, "GP workbench manual: Technical manual, user's guide, and software guide," *U.S. Geological Survey*, Open-File Report 2006-1365, 2007.
12. Smith, J. T. and H. F. Morrison, "Estimating equivalent dipole polarizabilities for the inductive response of isolated conductive bodies," *IEEE Trans. Geoscience and Remote Sensing*, Vol. 42, No. 6, 1208–1214, 2004.
13. Billings, S. D., L. R. Pasion, and D. W. Oldenburg, "Discrimination and identification of UXO by geophysical inversion," Technical Report, U.S. Army Research and Development Center, Vicksburg, MS, ERDC/GSL TR-02-16, 2002.
14. McFee, J. E., "Electromagnetic remote sensing: Low frequency electromagnetics," Technical Report 124, Defense Research Establishment Suffield, Ralston, Alberta, Canada, 1989.
15. Bruce, B., N. Khadr, R. DiMarco, and H. H. Nelson, "The combination use of magnetic and electromagnetic detection and characterization of UXO," *Symp. on the Application of Geophysics to Engineering & Environmental Problems*, Environmental and Engineering Geophysical Society, Denver, CO, Vol. 9, 469–478, 1996.

16. Snyder, D. D. and D. C. George, "Qualitative and quantitative UXO detection with EMI using arrays of multi-component receivers," *Symp. on the Application of Geophysics to Engineering & Environmental Problems*, Vol. 19, 1749–1760, Environmental and Engineering Geophysical Society, Denver, CO, 2006.
17. McDonald, J. R. and R. Robertson, "Sensor evaluation study for use with towed arrays for UXO site characterization," *Symp. on the Application of Geophysics to Engineering & Environmental Problems*, Vol. 9, 451–464, Environmental and Engineering Geophysical Society, Denver, CO, 1996.
18. Sylvester, P. P. and D. Omeragic, "Sensitivity of metal detectors to spheroidal targets," *IEEE Trans. Geoscience and Remote Sensing*, Vol. 33, No. 6, 1131–1335, 1995.
19. Wright, D. L., C. W. Moulton, T. H. Asch, P. J. Brown, M. N. Nabighian, Y. Li, and C. P. Oden, "Alltem UXO detection sensitivity and inversions for target parameters from Yuma proving ground test data," *Symp. on the Application of Geophysics to Engineering & Environmental Problems*, Environmental and Engineering Geophysical Society, Vol. 20, 1422–1435, Denver, CO, 2007.
20. Ward, S. H. and G. W. Hohmann, "Electromagnetic theory for geophysical applications, electromagnetic methods in applied geophysics," Vol. 1, Ch. 4, M. N. Nabighian Edition, Society of Exploration Geophysicists, Tulsa, OK, 1988.
21. Parise, M., "Fast computation of the forward solution in controlled-source electromagnetic sounding problems," *Progress In Electromagnetics Research*, Vol. 111, 119–139, 2011.
22. Anderson, W. L., "Computer program: Numerical integration of related Hankel transforms of orders 0 and 1 by adaptive digital filtering," *Geophysics*, Vol. 44, No. 7, 1287–1305, 1979.
23. Smith, J. T. and H. F. Morrison, "Approximating spheroid inductive responses using spheres," *Geophysics*, Vol. 71, No. 2, 21–25, 2006.
24. Das, Y., "Effects of soil electromagnetic properties on metal detectors," *IEEE Trans. Geoscience and Remote Sensing*, Vol. 44, No. 6, 1444–1453, 2006.
25. Pasion, L. R., S. D. Billings, D. W. Oldenburg, D. Sinex, and Y. Li, "Evaluating the effects of magnetic susceptibility in UXO discrimination problems," Final Report, Strategic Environmental Research and Development Program, SEED Project UX-1285, 2003.
26. Olhoeft, G. R. and D. W. Strangway, "Magnetic relaxation and

the electromagnetic response parameter," *Geophysics*, Vol. 39, No. 3, 302–311, 1974.

27. Vafeas, P., G. Perrusson, and D. Lesselier, "Low-frequency solution for a perfectly conducting sphere in a conductive medium with dipolar excitation," *Progress In Electromagnetics Research*, Vol. 49, 87–111, 2004.
28. Smith, J. T., H. F. Morrison, and A. Becker, "Parametric forms and the inductive response of a permeable conducting sphere," *J. Env. and Eng. Geoph.*, Vol. 9, No. 7, 213–216, 2004.
29. Zhou, G.-Q. and W.-J. Zhou, "The magnetic-moment quadric and conditions of vanishing magnetic moment for a rotational charged body," *Progress In Electromagnetics Research*, Vol. 70, 211–223, 2007.
30. Zhou, G.-Q., "Charge moment tensor and the magnetic moment of rotational charged bodies," *Progress In Electromagnetics Research*, Vol. 68, 151–160, 2007.
31. Wright, D. L., T. H. Asch, C. W. Moulton, T. P. Irons, and M. N. Nabighian, "Effects of spatial data density, sensor noise, and position errors on UXO and clutter target parameters from inversions of ALLTEM data," *Symp. on the Application of Geophysics to Engineering & Environmental Problems*, Vol. 21, 327–339, Environmental and Engineering Geophysical Society, Denver, CO, 2008.
32. Barrow, B. and H. H. Nelson, "Effects of positioning error on inverting EMI data for UXO discrimination using the MTADS platform," *Conference Proceedings on The UXO/Countermine Forum*, New Orleans, LA, 2001.
33. Smith, J. T. and H. F. Morrison, "Optimizing receiver configurations for resolution of equivalent dipole polarizabilities in-situ," *IEEE Trans. Geoscience and Remote Sensing*, Vol. 43, No. 7, 1490–1498, 2005.
34. Shubitidze, F., K. O'Neill, B. E. Barrowes, I. Shamatava, J. P. Fernández, K. Sun, and K. D. Paulsen, "Application of the normalized surface magnetic charge model to UXO discrimination in cases with overlapping signals," *J. Applied Geophysics*, Vol. 61, No. 3–4, 292–303, 2007.
35. Wright, D. L., C. W. Moulton, T. H. Asch, P. J. Brown, S. R. Hutton, M. N. Nabighian, and Y. Li, "ALLTEM for UXO applications — first field tests," *Symp. on the Application of Geophysics to Engineering & Environmental Problems*, Vol. 19, 1761–1775, Environmental and Engineering Geophysical Society, Denver, CO, 2006.